Weak Cubic $CaSiO_3$ Perovskite in Earth's Mantle

J. Immoor[1], L. Miyagi[2], H.-P. Liermann[3], S. Speziale[4], K. Schulze[5], J. Buchen[6], A. Kurnosov[1], H. Marquardt[7]*

[1]*Bayerisches Geoinstitut BGI, University of Bayreuth, 95440 Bayreuth, Germany;* [2]*University of Utah, 115 So. 1460 E., Salt Lake City, Utah 84112-0111, USA;* [3]*Photon Sciences, Deutsches Elektronen-Synchrotron (DESY), 22607 Hamburg, Germany;* [4]*German Research Center for Geosciences GFZ, 14473 Potsdam, Germany;* [5]*Materials Physics and Technology at Extreme Conditions, Laboratory of Crystallography, University of Bayreuth, 95440 Bayreuth, Germany;* [6]*Seismological Laboratory, California Institute of Technology, Pasadena, California, USA;* [7]*University of Oxford, Department of Earth Sciences, Oxford, OX1 3AN, United Kingdom*

**Correspondence to: Hauke.Marquardt@earth.ox.ac.uk*

Cubic $CaSiO_3$ perovskite is a major phase in subducted oceanic crust, where it forms at a depth of about 550 km from majoritic garnet[1,2]. We measured the plastic strength of cubic $CaSiO_3$ perovskite at pressure and temperature conditions typical for a subducting slab up to a depth of about 1200 km. Contrary to tetragonal $CaSiO_3$ previously investigated at room temperature[3,4], we find that cubic $CaSiO_3$ perovskite is a comparably weak phase at temperatures of the lower mantle. We find its viscosity to be substantially lower as compared to bridgmanite and ferropericlase, possibly making cubic $CaSiO_3$ perovskite the weakest lower mantle phase. Our findings suggest that cubic $CaSiO_3$ perovskite will govern the dynamics of subducting slabs. It further provides a mechanism to separate subducted oceanic crust from the underlying mantle. Depending on the depth of the separation, basaltic crust could accumulate at the boundary between the upper and lower mantle, where cubic $CaSiO_3$

perovskite may contribute to the seismically observed regions of low shear wave velocities in the uppermost lower mantle[5,6], or sink to the core-mantle boundary and explain the seismic anomalies associated with Large Low Shear Velocity Provinces LLSVPs beneath Africa and the Pacific[7-9].

$CaSiO_3$ perovskite is expected to be the third most abundant phase in Earth's transition zone and lower mantle, where it may account for up to 25 Vol.% of subducted basaltic crust and up to 10 Vol.% of a pyrolitic mantle[1,2]. Direct evidence for its existence has recently been reported from analysis of inclusions in super-deep diamonds[10]. At room temperature (T) and high pressure (P), $CaSiO_3$ perovskite has a tetragonal crystal structure, but undergoes a phase transition to a cubic structure with increasing temperature, stabilizing the cubic phase along a typical mantle geotherm[6,7,11,12]. It has been inferred that the elastic properties of cubic $CaSiO_3$ perovskite might explain regions of reduced shear wave velocities in the uppermost lower mantle[6] as well as some of the unique seismic properties of the Large Low Shear Velocity Provinces (LLSVP) observed by seismic tomography in the deep lower mantle[7-9].

While recent works succeeded to measure elastic wave velocities of cubic $CaSiO_3$ perovskite at high-pressure/-temperature[6,7], experimental information on its rheology is absent. Previous studies of the deformation behavior of $CaSiO_3$ are limited to its tetragonal polymorph at room T (refs. 3,4) due to experimental difficulties preventing access to mantle-like P-T-conditions. These works suggest that $CaSiO_3$ perovskite is characterized by a high plastic strength, exceeding that of $MgSiO_3$ bridgmanite, the dominant phase in Earth's lower mantle. Early computational work, however, predicted that the lattice friction, i.e. the Peierls stress, of the <110>{1-10} slip system

47 in cubic $CaSiO_3$ perovskite is almost zero[13], which appears incompatible with a very large plastic
48 strength. Theoretical work further suggested that the Peierls stress increases with structural
49 distortions in perovskite-structured materials[14]. The deformation behavior of cubic $CaSiO_3$
50 perovskite might thus markedly differ from that of its tetragonal counterpart.
51
52 Here, we synthesized and deformed cubic $CaSiO_3$ perovskite at 1150(±50) K (Fig. 1) in a recently
53 developed high-pressure/-temperature apparatus[15] using synchrotron-based radial x-ray diffraction
54 at the Extreme Conditions Beamline, P02.2, at PETRA III, DESY, Hamburg, Germany. High-
55 pressure lattice strains, *Q(hkl)*, were extracted from the recorded diffraction images by fitting the
56 experimental observations using the program MAUD (See Methods) where *hkl* refers to the Miller
57 indices of the respective lattice planes. The deviatoric stress *t* supported by the sample was
58 calculated from the average of measured lattice strains using the identity $t = 6 \cdot \langle Q(hkl) \rangle \cdot G$, where
59 the high-pressure shear modulus, *G*, at 1150 K was taken from ref. 7. Texture development was
60 observed in $CaSiO_3$ perovskite throughout the experiment. The observation of texture development
61 throughout the experiment, as well as plasticity modelling, shows that plastic deformation occurred
62 in the sample (Extended Data Figures 3, 4) and measured stresses can thus be treated as
63 approximations for the sample's plastic strength[16]. The observed texture strength in our high-
64 temperature experiments is higher than in previous experiments at room temperature[3], a result of
65 the sample's lower strength.
66
67 In Fig. 2, we compare the here-derived high-temperature strength of cubic $CaSiO_3$ perovskite to
68 previously derived values for (Mg,Fe)O ferropericlase[17] and bridgmanite[18,19], as well as to reported
69 strengths at room temperature[3,20,21]. We note that almost all shown values have been determined

by radial x-ray diffraction in the diamond-anvil cell, permitting a direct comparison. Strikingly, cubic $CaSiO_3$ perovskite is characterized by a high-temperature plastic strength that is substantially lower than that reported for bridgmanite and even ferropericlase, which has previously been regarded as the weakest major lower mantle phase[19,21-23], only possibly rivalled by post-perovskite below ~2500 km depth[24]. It is striking that the strength of $CaSiO_3$ measured here at 1150 K is substantially lower than the strength of bridgmanite previously drrived at 2750 K (at 27.5 GPa)[19]. A particularly interesting observation is the large strength contrast between tetragonal $CaSiO_3$ measured at 295 K (Fig. 2a) and cubic $CaSiO_3$ perovskite at 1150 K (Fig. 2b). While strength is expected to decrease with temperature, the here-observed decrease is much larger than expected from a rise in temperature alone as evident by comparison to ferropericlase and bridgmanite (Fig. 2). It appears likely that the tetragonal lattice distortion experienced by $CaSiO_3$ perovskite upon temperature decrease leads to an additional increase in strength. This observation is qualitatively consistent with computational work predicting Peierls stresses to increase with lattice distortions in perovskite-structured materials[14].

We use the here-derived strength values together with the previous results shown in Fig. 2 to estimate the viscosity contrast between cubic $CaSiO_3$ perovskite, bridgmanite and ferropericlase in the lower mantle. While our measurements have been performed at pressure and temperature conditions typical for the slab's interior at shallow lower-mantle conditions, a major difference between our experiments and deformation in Earth's mantle is the strain rate and the magnitude of stress. Assuming that the observed rheological behavior is governed by a dislocation-dominated process as expected for high strain rates in both our experiments and subducted slabs in Earth's mantle, it can be described by

$\dot{\varepsilon} = A \cdot \sigma^n$, where $\dot{\varepsilon}$ is the strain rate, σ is stress, n is the stress exponent, and A is a pre-factor.

We used the identity above, together with the definition of viscosity $\eta = \sigma/2\dot{\varepsilon}$, to calculate viscosity ratios between the major lower mantle phases bridgmanite, ferropericlase, and $CaSiO_3$ perovskite using the strength values in Fig. 2b. Initially, we assumed that the strain rates in all experiments were the same (10^{-4} s^{-1}, ref. [21]) and that samples were deformed by similar processes and hence are described by the same stress exponent (3-5). However, deviations from these assumptions were tested (see Extended Data Table 1). Under these assumptions, the calculated viscosity ratios are independent of the values chosen for mantle stress and strain rate, and only mildly sensitive to the chosen stress exponent (Fig. 3, see also Methods).

Fig. 3 shows two endmember scenarios assuming either uniform strain rate or stress throughout the aggregate. Fig. 3a reflects a situation where the rock deforms as a whole and strain rate is uniform, a situation that is characteristic for a load-bearing framework (LBF) type deformation. Fig. 3b reflects a situation where strain partitions in the weaker phase and stress is thus equally distributed between the phases, a situation that is characteristic for an interconnected weak layer (IWL) type deformation. Cubic $CaSiO_3$ perovskite is always the weakest mantle phase and often shows a viscosity that is several orders of magnitude smaller as compared to bridgmanite and ferropericlase. At 1000 km depths, corresponding to a pressure of about 40 GPa where experimental results for all phases are available, we find cubic $CaSiO_3$ to have a viscosity that is 1.4 to 4 orders of magnitude lower as compared to bridgmanite and 1 to 3 order of magnitude lower than ferropericlase (for n = 3). The viscosity contrast is particularly pronounced for the IWL scenario, which is likely to

develop in large strain regions of the mantle. To test the robustness of our findings, we evaluated the effect of assuming different experimental strain rates and stress exponents for bridgmanite, ferropericlase, and $CaSiO_3$ perovskite (see Methods). We found that viscosities consistently increased from $CaSiO_3$ perovskite to ferropericlase to bridgmanite for a wide range of model parameters. We note that the calculation of viscosity contrasts by necessity involves several assumptions and relies on poorly constrained parameters as detailed in Methods, future experimental and theoretical work might aim to better quantify these. The presence of hydrogen in the lower mantle might further affect the rheological behavior of $CaSiO_3$ perovskite (and bridgmanite), even though a recent study showed that the effect might be rather small[25].

The presence of weak cubic $CaSiO_3$ perovskite has wide-ranging consequences for the dynamics of subducting slabs and the interpretation of seismic observations. The formation of $CaSiO_3$ perovskite from majoritic garnet, a comparably hard phase[26], at around 550 km depth in subducted oceanic crust[27] will lead to a substantial weakening of the oceanic crust. Previous works on two-phase deformation of a bridgmanite–ferropericlase assemblage, a proxy for a lower mantle rock, have predicted that strain starts to partition into the weak ferropericlase that can form an IWL network during deformation, thereby lowering the viscosity of the two-phase assemblage by several orders of magnitude[19,21-23,28]. However, the onset of strain localization largely depends on the viscosity contrast between the phases and the volume fraction of the weak phase[23]. Our results suggest that the viscosity contrast between bridgmanite and cubic $CaSiO_3$ perovskite is substantially larger as compared to the one between bridgmanite and ferropericlase. Moreover, the volume fraction of $CaSiO_3$ perovskite in subducted oceanic crust is larger than the ferropericlase fraction in a pyrolitic lower mantle rock.

Taken this together, we expect strain localization to occur in subducted oceanic crust after the onset of cubic $CaSiO_3$ perovskite formation. $CaSiO_3$ perovskite gradually forms with depths from majoritic garnet and its volume fraction continuously increases between about 500 km and 700 km depth[27]. Once the interconnection volume threshold is reached and the accumulated strain is sufficiently large, strain will start to partition between phases and an IWL network will develop, leading to marked weakening of the crustal part of the subducted slab. Deformation of the crust will initially be governed by a LBF of the hard phase(s), which depending on depth are majoritic garnet, bridgmanite, and stishovite[29]. In this scenario, the effective viscosity contrast can be approximated by a constant strain rate assumption (Fig. 3a). With increasing deformation, strain will start to partition into the weak $CaSiO_3$ phase, leading to rock weakening and initiating a continuous transition towards a deformation scenario where stress is equally distributed between all phases (Fig. 3b). The increase in effective viscosity contrasts between the phases that is caused by this transition will accelerate strain partitioning, further weakening the subducted crust.

Since we expect cubic $CaSiO_3$ perovskite to form and strain to build up from around 550 km depth, we speculate that the strain weakening effect in subducted oceanic crust will already be significant at the time of bridgmanite and ferropericlase formation at around 660 km depth in the surrounding mantle. The weak layer of subducted oceanic crust would thus be sandwiched between comparably hard mantle rocks and could easily be separated from the surrounding mantle by shear forces[30], similar to weak sediments in the shallower parts of subduction zone. At depths between 660 km and 720 km depths, basaltic oceanic crust is less dense than ambient mantle[31], but below about 720 km, after garnet has completely dissolved into perovskite-structured phases, oceanic crust becomes denser than ambient mantle[31,32]. Depending on the depth-dependent buoyancy contrast to the

surrounding mantle, low-viscosity oceanic crust could thus segregate and accumulate around 660 km depth[5] or migrate towards the core-mantle boundary, behaving like an "upside-down plume". The low viscosity of cubic $CaSiO_3$ perovskite provides an intrinsic mechanism to separate slab materials and to accumulate recycled oceanic crust either at the boundary between the upper and lower mantle or at the core-mantle boundary, where cubic $CaSiO_3$ perovskite may contribute to seismically observed regions of low shear wave velocities in the uppermost lower mantle[5] as well as the LLSVPs beneath Africa and the Pacific as hypothesized earlier[7-9]. Deep recycling of oceanic crust has further been inferred to contribute to the geochemical diversity observed in ocean island basalts at the surface[33].

The above-mentioned implications require the presence of cubic $CaSiO_3$ perovskite and hence the tetragonal-cubic transition to occur at temperatures below the geotherm[7,11]. If lower mantle $CaSiO_3$ perovskite contains titanium or aluminium as suggested by the analysis of a diamond inclusion[10], the tetragonal-cubic transition is shifted to higher temperatures[7,11,34], possibly intersecting a cold subduction geotherm[7]. The tetragonal-cubic transition could then lead to sudden changes of rheological properties which would affect the dynamic behavior of a subducting slab, possibly leading to slab buckling, delamination and/or stagnation. The dependence of this dynamic change on the availability of titanium and aluminum could help explain the diverse behavior of slabs in the lower mantle[35]. Details of the interaction of a weak subducting crust, as indicated by our experiments, with the surrounding mantle should be explored by future geodynamic modelling, as should be the effect of the presence of an Al-bearing phase in subducted oceanic crust that might further complicate slab rheology.

References

1 Irifune, T. & Tsuchiya, T. Mineralogy of the Earth - Phase transitions and mineralogy of the lower mantle. in *Treatise on Geophysics* **2**, 33-62 (2007).

2 Hirose, K., Sinmyo, R. & Hernlund, J. Perovskite in Earth's deep interior. *Science* **358**, 734-738 (2017).

3 Miyagi, L. *et al.* Diamond anvil cell deformation of $CaSiO_3$ perovskite up to 49 GPa. *Phys. Earth Planet. Inter.* **174**, 159-164 (2009).

4 Shieh, S. R., Duffy, T. S. & Shen, G. Elasticity and strength of calcium silicate perovskite at lower mantle pressures. *Phys. Earth Planet. Inter.* **143-144**, 93-105 (2004).

5 Ballmer, M. D., Schmerr, N. C., Nakagawa, T. & Ritsema, J. Compositional mantle layering revealed by slab stagnation at ~1000-km depth. *Science Advances* **1** (2015).

6 Gréaux, S. *et al.* Sound velocity of $CaSiO_3$ perovskite suggests the presence of basaltic crust in the Earth's lower mantle. *Nature* **565**, 218-221 (2019).

7 Thomson, A. *et al.* Calcium silicate perovskite's acoustic velocities can explain LLSVPs in Earth's lower mantle. *Nature* **572**, 643-647 (2019).

8 Jones, T. D., Maguire, R. R., van Keken, P. E., Ritsema, J. & Koelemeijer, P. Subducted oceanic crust as the origin of seismically slow lower-mantle structures. *Progress in Earth and Planetary Science* **7**, 17 (2020).

9 Garnero, E. J., McNamara, A. K. & Shim, S.-H. Continent-sized anomalous zones with low seismic velocity at the base of Earth's mantle. *Nat. Geosci.* **9**, 481-489 (2016).

10 Nestola, F. *et al.* CaSiO3 perovskite in diamond indicates the recycling of oceanic crust into the lower mantle. *Nature* **555**, 237 (2018).

11 Komabayashi, T., Hirose, K., Sata, N., Ohishi, Y. & Dubrovinsky, L. S. Phase transition in $CaSiO_3$ perovskite. *Earth and Planetary Science Letters* **260**, 564-569 (2007).

12 Sun, N. *et al.* Confirming a pyrolitic lower mantle using self-consistent pressure scales and new constraints on CaSiO3 perovskite. *Journal of Geophysical Research: Solid Earth* **121**, 4876-4894 (2016).

13 Ferré, D., Cordier, P. & Carrez, P. Dislocation modeling in calcium silicate perovskite based on the Peierls-Nabarro model. *American Mineralogist* **94**, 135-142 (2009).

14 Ferré, D., Carrez, P. & Cordier, P. Peierls dislocation modelling in perovskite (CaTiO3): comparison with tausonite (SrTiO3) and MgSiO3 perovskite. *Physics and Chemistry of Minerals* **36**, 233-239 (2009).

15 Immoor, J. *et al.* An improved setup for radial diffraction experiments at high pressures and high temperatures in a resistive graphite-heated diamond anvil cell. *Review of Scientific Instruments* **91**, 045121 (2020).

16 Merkel, S. *et al.* Deformation of polycrystalline MgO at pressures of the lower mantle. *J. Geophys. Res.* **107**, 2271 (2002).

17 Immoor, J. *et al.* Evidence for {100}<011> slip in ferropericlase in Earth's lower mantle from high-pressure/high-temperature experiments. *Earth and Planetary Science Letters* **489**, 251-257 (2018).

18 Couper, S., Speziale, S., Marquardt, H., Liermann, H. P. & Miyagi, L. Does Heterogeneous Strain Act as a Control on Seismic Anisotropy in Earth's Lower Mantle? *Frontiers in Earth Science* **8**, 540449. doi: 540410.543389/feart.542020.540449 (2020).

19 Girard, J., Amulele, G., Farla, R., Mohiuddin, A. & Karato, S.-i. Shear deformation of bridgmanite and magnesiowüstite aggregates at lower mantle conditions. *Science* **351**, 144-147 (2016).

20 Merkel, S. *et al.* Deformation of $(Mg_{0.9}Fe_{0.1})SiO_3$ Perovskite aggregates up to 32 GPa. *Earth and Planetary Science Letters* **209**, 351-360 (2003).

21 Marquardt, H. & Miyagi, L. Slab stagnation in the shallow lower mantle linked to an increase in mantle viscosity. *Nat. Geosci.* **8**, 311-314 (2015).
22 Yamazaki, D. & Karato, S.-i. Some mineral physics constraints on the rheology and geothermal structure of Earth's lower mantle. *American Mineralogist* **86**, 385-391 (2001).
23 Thielmann, M., Golabek, G. J. & Marquardt, H. Ferropericlase Control of Lower Mantle Rheology: Impact of Phase Morphology. *Geochem. Geophys. Geosys.* **21**, e2019GC008688 (2020).
24 Goryaeva, A. M., Carrez, P. & Cordier, P. Low viscosity and high attenuation in MgSiO3 post-perovskite inferred from atomic-scale calculations. *Sci Rep* **6**, 34771 (2016).
25 Muir, J. M. R. & Brodholt, J. P. Water distribution in the lower mantle: Implications for hydrolytic weakening. *Earth and Planetary Science Letters* **484**, 363-369 (2018).
26 Kavner, A., Sinogeikin, S. V., Jeanloz, R. & Bass, J. D. Equation of state and strength of natural majorite. *Journal of Geophysical Research: Solid Earth* **105**, 5963-5971 (2000).
27 Saikia, A., Frost, D. J. & Rubie, D. C. Splitting of the 520-Kilometer Seismic Discontinuity and Chemical Heterogeneity in the Mantle. *Science* **319**, 1515-1518 (2008).
28 Takeda, Y.-T. Flow in rocks modelled as multiphase continua: application to polymineralic rocks. *J Struc Geol* **20**, 1569-1578 (1998).
29 Hunt, S. A. *et al.* An Experimental Investigation of the Relative Strength of the Silica Polymorphs Quartz, Coesite, and Stishovite. *Geochem. Geophys. Geosys.* **20**, 1975-1989 (2019).
30 van Keken, P. E., Karato, S. & Yuen, D. A. Rheological control of oceanic crust separation in the transition zone. *Geophysical Research Letters* **23**, 1821-1824 (1996).
31 Hirose, K., Fei, Y., Ma, Y. & Mao, H.-K. The fate of subducted basaltic crust in the Earth's lower mantle. *Nature* **397**, 53-56 (1999).
32 Hirose, K., Takafuji, N., Sata, N. & Ohishi, Y. Phase transition and density of subducted MORB crust in the lower mantle. *Earth and Planetary Science Letters* **237**, 239-251 (2005).
33 Hofmann, A. W. Mantle geochemistry; the message from oceanic volcanism. *Nature* **385**, 219-229 (1997).
34 Kurashina, T., Hirose, K., Ono, S., Sata, N. & Ohishi, Y. Phase transition in Al-bearing $CaSiO_3$ perovskite: implications for seismic discontinuities in the lower mantle. *Phys. Earth Planet. Inter.* **145**, 67-74 (2004).
35 Fukao, Y. & Obayashi, M. Subducted slabs stagnant above, penetrating through, and trapped below the 660 km discontinuity. *J. Geophys. Res.* **118**, 2013JB010466 (2013).

Acknowledgements: We acknowledge technical assistance by A. Ehnes and I. Schwark. We thank Andrew Thomson for providing a table with the high-temperature shear modulus of $CaSiO_3$ perovskite. This research was supported through the German Science Foundation (grants MA4534/3-1 and MA4534/4-1) as well the European Union's Horizon 2020 research and innovation Programme (ERC grant 864877). HM acknowledges support from the Bavarian Academy of Sciences. L.M. acknowledges support from the NSF (EAR-1654687) and US Department of Energy National Nuclear Security Administration through the Chicago-DOE Alliance Center (DE- NA0003975).

Author contributions: HM, HPL, LM, SS designed the research. JI prepared the experiments. All author contributed to the Synchrotron experiments. JI and LM analysed the data. HM performed the modelling. HM wrote the initial draft of the manuscript. All authors contributed to the final writing of the manuscript.

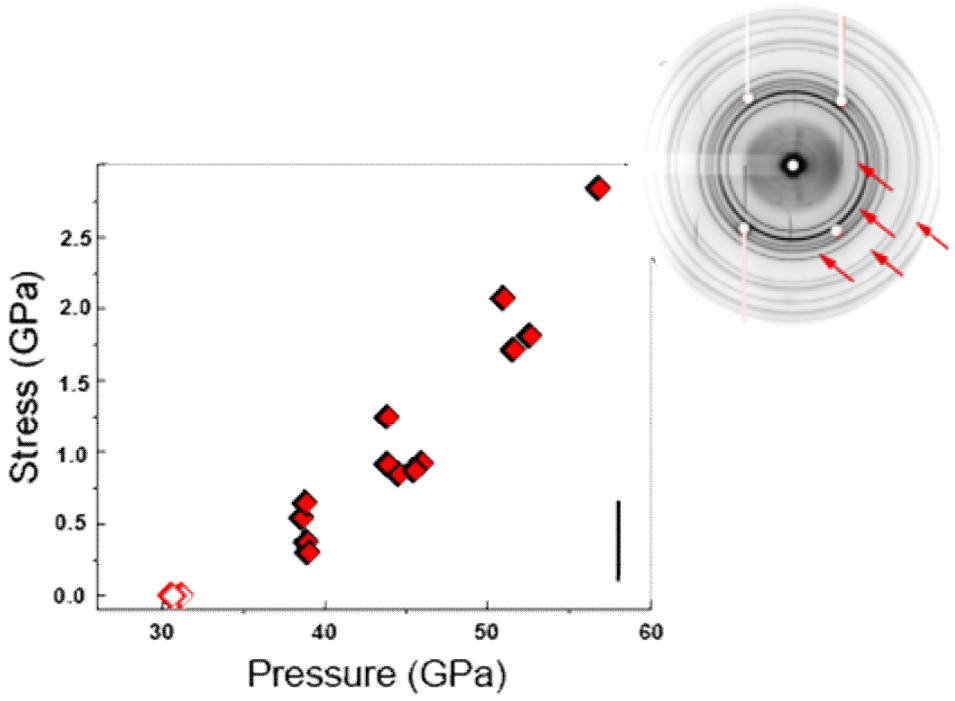

Figure 1. Deviatoric stress measured in cubic $CaSiO_3$ perovskite at lower mantle pressures and T = 1150(±50) K. Texture development is observed from 39 GPa (see Methods), indicating plastic flow. Inset shows a typical diffraction pattern collected after *in-situ* high-pressure/high-temperature synthesis of cubic $CaSiO_3$ perovskite in the diamond-anvil cell showing Debye rings of cubic $CaSiO_3$ (green coloured rings) and platinum (blue coloured rings). Open symbols denote data that have been collected shortly after synthesis and have been excluded from the strength calculation. The size of the experimental errors, propagated from the uncertainties in measured Q-values, is indicated by the bar in the lower right corner.

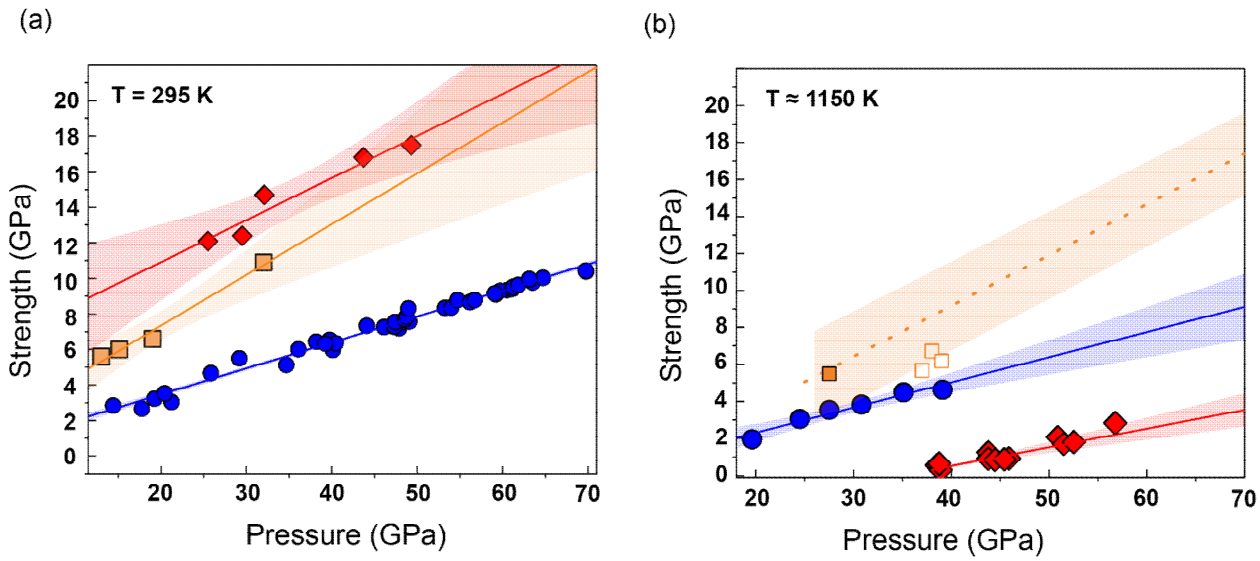

Figure 2. Strength of major lower mantle phases at high pressures. (a) Strength values measured at room temperature by previous works. Red: (tetragonal) $CaSiO_3$ perovskite[3]; orange: $Mg_{0.9}Fe_{0.1}SiO_3$ bridgmanite[20]; blue: $(Mg_{0.8}Fe_{0.2})O$ ferropericlase[21]. (b) Here-derived high-temperature strength of cubic $CaSiO_3$ perovskite at lower mantle pressures (red solid diamonds) compared to the strength of $(Mg_{0.8}Fe_{0.2})O$ measured at 1150 K (blue solid circles)[17] and the stress measured on bridgmanite deformed as part of a multi-phase assemblage at 1000 K at comparably low strains, likely representing a lower bound to the high-temperature strength of bridgmanite (open squares)[18]. The solid orange square denotes the strength of bridgmanite at 2750 K, taken from ref. 19 (their run "gamma 25"). Best-fit lines are shown along with their 95% confidence range. Given the limited amount of data on the high-temperature strength reported for bridgmanite, the strength of bridgmanite at 1150 K was derived from the data measured for bridgmanite at 295 K[20] by applying two different temperature corrections represented by the shaded region (see Methods). Even though we acknowledge that this procedure is uncertain, the overlap of our derived range with the data collected on two-phase samples (squares) suggest that it provides a reasonable estimate.

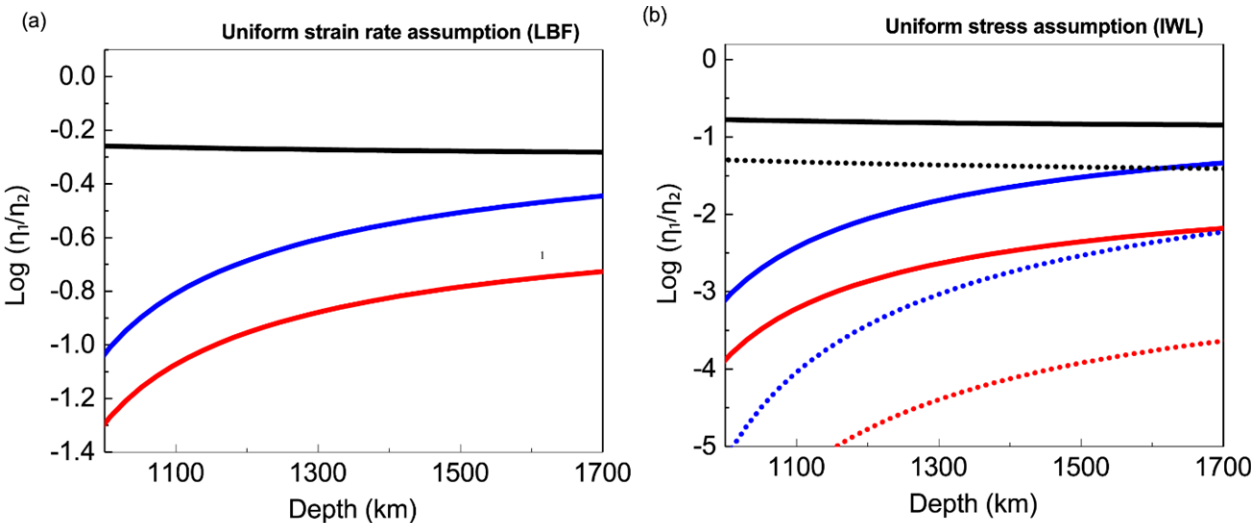

311

312 **Figure 3. Depth-dependent viscosity contrast between major lower mantle phases at ~1150**
313 **K.** The viscosity contrast is shown for pairs of mantle phases of viscosity η_1 and η_2. Red curve:
314 η_{CaSiO3}/η_{Bm}; Blue curve: η_{CaSiO3}/η_{Fp}; Black curve: η_{Fp}/η_{Bm}. (a) viscosity contrast calculated under
315 the assumption that strain rate is equal in both phases. This assumption represents the stage of
316 initial deformation which is dominated by a load-bearing framework (LBF) of the harder phase.
317 (b) Viscosity contrast calculated for a uniform stress assumption, representing a scenario of
318 progressed deformation that has led to the development of an interconnected weak layer (IWL) of
319 the weak phase. Calculations have been performed with a stress exponent $n = 3$ (solid curves) and
320 $n = 5$ (dotted curves).

Methods:

Experimental details:

A resistive-heated diamond-anvil cell (DAC), based on a customised Mao-Bell-type DAC and designed for radial x-ray diffraction experiments, was used for the experiments[1]. Diamonds with culet sizes of 300 µm were employed, together with a gasket made of an amorphous boron epoxy mixture that was inserted in a Kapton foil. A resistive-heater that surrounds the diamond tips was made of two thin flexible graphite layers that are in tight contact with the diamond anvils. To allow x-rays to pass through the heater, a beam path was carved into the graphite sheets[1,2]. The entire DAC was positioned inside a vacuum chamber designed at the Extreme Condition Beamline (ECB, P02.2) at PETRA III of the Deutsches Elektronen Synchrotron (DESY)[1,3]. During the experiments, a vacuum of better then 10^{-4} mbar was maintained to avoid oxidation of the cell and diamonds. The outside of the vacuum chamber was kept at low temperatures by a water-cooling system[1,3]. The starting material was finely-ground powder of $CaSiO_3$ wollastonite mixed with a small amount of fine-powdered platinum to determine the experimental pressure employing previously published thermal equation of state parameters[4]. The sample was heated at a pressure of ~30 GPa, until the appearance of new diffraction rings indicated the formation of $CaSiO_3$ perovskite (Fig. 1). Temperature was increased slowly (hours) to allow the system to equilibrate and maintain the vacuum. Pressure was then increased at a constant temperature of 1150(±50) K, leading to the deformation of the sample. Temperature was determined as the average of the measurement of two thermocouples placed between the heater and below the gasket[1], with the given uncertainty reflecting the difference between the two measurements. Pressure was increased remotely using a gas-membrane system and diffraction images were taken after pressure stabilized. X-ray diffraction experiments were performed at the Extreme Conditions Beamline (ECB) P02.2 at PETRA III at DESY[3]. X-rays with an energy of 25 keV were focused to 8 (h) x 3 (v) µm². The diffraction images were

recorded on a Perkin Elmer XRD 1621 flat panel detector, sliced using Fit2d software[5] and analysed using the software package MAUD[6] (Extended Data Figure 1). The "radial diffraction in the DAC" model[7] was used to fit lattice strains (110, 111, 200, 211 reflections) in $CaSiO_3$ perovskite. The E-WIMW model which is similar to the WIMV model[8], but allows for incomplete and arbitrary pole figure coverage was employed to fit textures. Cylindrical symmetry was imposed. The orientation distribution function (ODF) was exported to BEARTEX[9] to plot Inverse Pole Figures (IPF). Derived lattice strains and texture evolution are shown in Extended Data Figs. 2 and 3. A clear texture development is observed throughout the experiment, where texture strength increased from 1.5 multiples of random distribution (mrd) after synthesis to about 1.75 mrd at the highest pressures. It is important to note that both the sample's strength and texture are derived from the same set of grains sampled by the x-rays. It is therefore not possible by experimental design that some highly stressed grains that cause texture development are missing from our strength measurement.

Visco-Plastic Self-Consistent (VPSC) Modelling of Texture Development

We performed Visco-Plastic Self-Consistent (VPSC) simulations[10] to model slip system activites and to determine the amount of plastic strain required to reproduce the experimentally measured increase of texture strength (Extended Data Figure 4). Simulations were performed using VPSC version 6 with a tangent approximation for the inclusion matrix interaction. The starting texture was discretized into 3000 grains from the experimentally measured ODF at 31.1 GPa. This was then used as the starting texture for plasticity simulations. Different amounts of strain were applied in the simulation until the texture strength measured at 52.2 GPa was reproduced by the model. The best-fit model required 20% plastic strain with dominant 110 slip (79% of total strain is on 110).

Modelling of the strength of bridgmanite at 1150 K and lower mantle pressures:

In absence of direct measurements of the plastic strength of single-phase bridgmanite at relevant pressures and high temperatures, we applied a temperature correction to 295 K DAC experiments[11]. We used the average value of two different approaches, where (1) the effect of temperature on the strength of bridgmanite is assumed to be the same as that measured for ferropericlase, (2) the 295 K results were shifted to lower strength values to match those measured for bridgmanite deformed in a DAC within a multi-phase assemblage[12].

Modelling of viscosity contrast between lower mantle phases:

We used our experimental data to calculate viscosity contrasts between major lower mantle phases using the identities:

$$\dot{\varepsilon} = A \cdot \sigma^n \qquad (1)$$

and

$$\eta = \sigma/2\dot{\varepsilon} \qquad (2)$$

Here, η is viscosity, $\dot{\varepsilon}$ is the strain rate, σ is stress, n is the stress exponent, and A is a pre-factor.

The above relations can be combined to calculate the viscosity contrast between any two phases (denoted by subscripts) for either a uniform stress or uniform strain rate scenario, according to:

$$\frac{\eta_1}{\eta_2} = \frac{\dot{\varepsilon}_2 \cdot {\sigma_1}^{n_1}}{\dot{\varepsilon}_1 \cdot {\sigma_2}^{n_2}} \cdot \sigma_g^{(n_2 - n_1)} \qquad \text{(for uniform geophysical stress } \sigma_g\text{)} \qquad (3)$$

$$\frac{\eta_1}{\eta_2} = \frac{{A_2}^{\left(\frac{1}{n_2}\right)}}{{A_1}^{\left(\frac{1}{n_1}\right)}} \cdot \dot{\varepsilon}_g^{\left(\frac{1}{n_1} - \frac{1}{n_2}\right)} \qquad \text{(for uniform geophysical strain rate } \dot{\varepsilon}_g\text{)} \qquad (4)$$

Under the assumption that the strain rates in all experiments were the same and samples deformed by similar processes and hence are described by the same stress exponent *n*, the above equations can be simplified to

$$\frac{\eta_1}{\eta_2} = \left(\frac{\sigma_1}{\sigma_2}\right)^n \quad \text{(for uniform geophysical stress)} \qquad (5)$$

$$\frac{\eta_1}{\eta_2} = \frac{\sigma_1}{\sigma_2} \quad \text{(for uniform geophysical strain rate)} \qquad (6)$$

To test the effect of this simplification on the here-derived viscosity contrasts (Fig. 3), we used equations (3) and (4) to test the effect of different stress exponents for the three mantle minerals and differences in experimental strain rates over a relevant range. The results are summarized in Extended Data Table 1. We find that cubic $CaSiO_3$ consistently shows a lower viscosity than both bridgmanite and ferropericlase, often by several orders of magnitude. It shows a particularly low viscosity in our uniform stress models.

Extended Data:

Extended Data Table 1: Viscosity contrast between $CaSiO_3$ perovskite and bridgmanite (left) or ferropericlase (right) calculated from strength values at 40 GPa and ~1150 K (see Fig. 2b). The effect of varying the stress exponent and experimental strain rate on calculated viscosity contrasts was tested. In calculating the values in the table, we assumed a stress exponent of 4 and an experimental strain rate of 10^{-4} s^{-1} for $CaSiO_3$. We further fixed the mantle stress to 10 MPa and the mantle strain rate to 10^{-14} s^{-1} for calculations at uniform stress and strain rate, respectively.

$CaSiO_3$ perovskite / bridgmanite				$CaSiO_3$ perovskite / ferropericlase			
n_{Bm}	$\dot{\varepsilon}_{Bm}$ (s^{-1})	$LOG(\eta_{CaSiO3}/\eta_{Bm})$		n_{Fp}	$\dot{\varepsilon}_{Fp}$ (s^{-1})	$LOG(\eta_{CaSiO3}/\eta_{Fp})$	
		σ_g = constant	$\dot{\varepsilon}_g$ = constant			σ_g = constant	$\dot{\varepsilon}_g$= constant
3	10^{-3} – 10^{-5}	-5.9 to -3.9	-0.1 to -0.7	3	10^{-3} – 10^{-5}	-5.1 to -3.1	-0.5 to 0.2
4	10^{-3} – 10^{-5}	-5.8 to -3.8	-1.5 to -1.0	4	10^{-3} – 10^{-5}	-4.8 to -2.8	-1.2 to -0.7
5	10^{-3} – 10^{-5}	-5.8 to -3.8	-1.9 to -1.5	5	10^{-3} – 10^{-5}	-4.5 to -2.5	-1.7 to -1.3

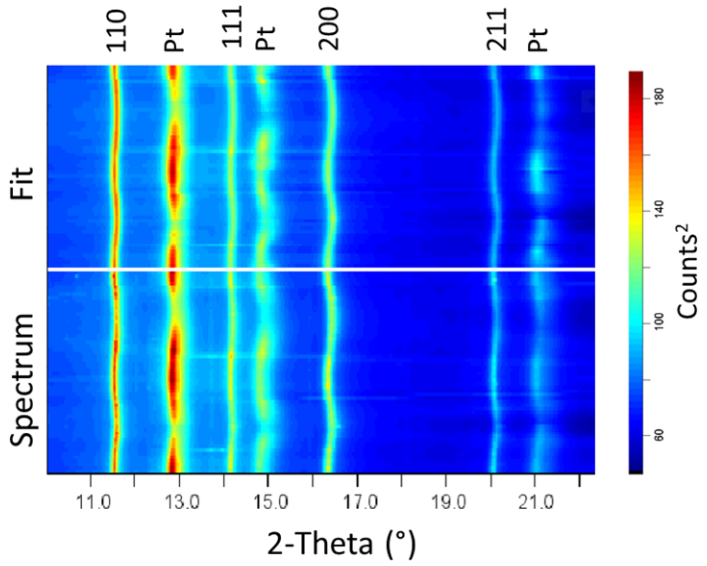

Extended Data Figure 1: Unrolled diffraction image collected at 52.5 GPa and 1150(±50) K (bottom) along with the best-fit model (top). The curvature is a measure of lattice strains and was used to calculate the strength of $CaSiO_3$ perovskite.

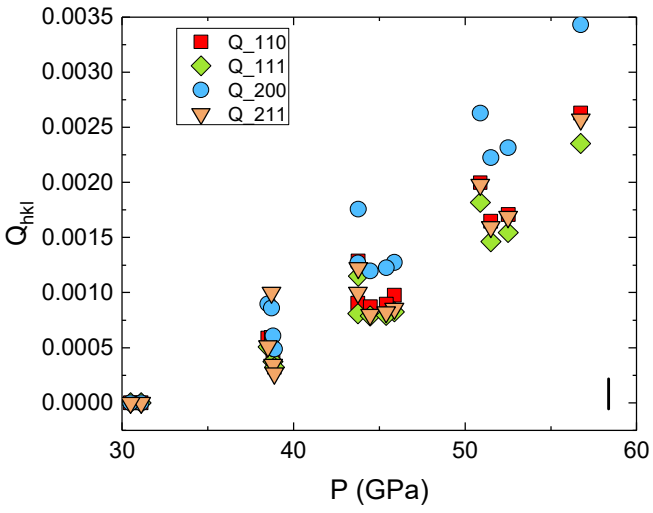

Extended Data Figure 2: Experimentally derived lattice strains of cubic $CaSiO_3$ at a temperature of 1150(±50) K. The error of the derived lattice strains is similar to the symbol sizes as shown in the lower right corner.

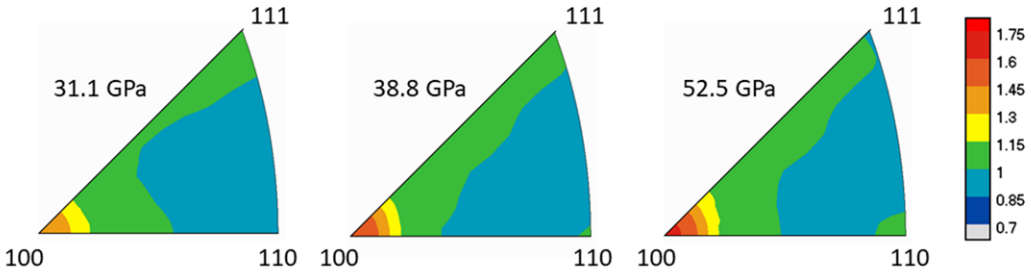

Extended Data Figure 3: Texture development observed in experiments. Texture strength is indicated by the colours. 100 texture increases with pressure throughout the experiment, increasing from about 1.5 mrd to 1.75 mrd, indicating plastic flow.

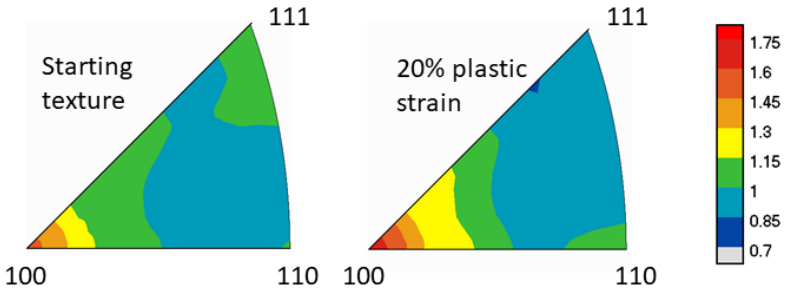

Extended Data Figure 4: VPSC modelling of texture development. The measured experimental texture after sample synthesis was used as starting texture. 20% of plastic strain leads to a texture strength comparable to the one measured at 52.2 GPa (see Extended Data Figure 3).

References

1 Immoor, J. *et al.* An improved setup for radial diffraction experiments at high pressures and high temperatures in a resistive graphite-heated diamond anvil cell. *Review of Scientific Instruments* **91**, 045121 (2020).

2 Liermann, H.-P. *et al.* Experimental method for in situ determination of material textures at simultaneous high pressure and high temperature by means of radial diffraction in the diamond anvil cell. *Review of scientific instruments* **80**, 104501 (2009).

3 Liermann, H.-P. *et al.* The Extreme Conditions Beamline P02.2 and the Extreme Conditions Science Infrastructure at PETRA III. *J. of Synchr. Rad.* **22**, 908-924 (2015).

4 Fei, Y. *et al.* High-Pressure Geoscience Special Feature: Toward an internally consistent pressure scale. *Proc. Natl. Acad. Sci.* **104**, 9182-9186 (2007).

5 Hammersley, A. P., Svensson, S. O., Hanfland, M., Fitch, A. N. & Hausermann, D. Two-dimensional detector software: From real detector to idealised image or two-theta scan. *High Press. Res.* **14**, 235-248 (1996).

6 Lutterotti, L., Matthies, S., Wenk, H.-R., Schultz, A. S. & Richardson, J. W. Combined texture and structure analysis of deformed limestone from time-of-flight neutron diffraction spectra. *Journal of Applied Physics* **81**, 594-600 (1997).

7 Singh, A. K., Balasingh, C., Mao, H.-k., Hemley, R. J. & Shu, J. Analysis of lattice strains measured under nonhydrostatic pressure. *Journal of Applied Physics* **83**, 7567-7575 (1998).

8 Matthies, S. & Vinel, G. W. On the Reproduction of the Orientation Distribution Function of Texturized Samples from Reduced Pole Figures Using the Conception of a Conditional Ghost Correction. *Phys. Status Solidi B* **112**, K111-K114 (1982).

9 Wenk, H. R., Matthies, S., Donovan, J. & Chateigner, D. BEARTEX: a Windows-based program system for quantitative texture analysis. *J. Appl. Crystallogr.* **31**, 262-269 (1998).

10 Lebensohn, R. A. & Tomé, C. N. A self-consistent anisotropic approach for the simulation of plastic deformation and texture development of polycrystals: Application to zirconium alloys. *Acta Metall. Mater.* **41**, 2611-2624 (1993).

11 Merkel, S. *et al.* Deformation of $(Mg_{0.9}Fe_{0.1})SiO_3$ Perovskite aggregates up to 32 GPa. *Earth and Planetary Science Letters* **209**, 351-360 (2003).

12 Couper, S., Speziale, S., Marquardt, H., Liermann, H. P. & Miyagi, L. Does Heterogeneous Strain Act as a Control on Seismic Anisotropy in Earth's Lower Mantle? *Frontiers in Earth Science* **8**, 540449. doi: 540410.543389/feart.542020.540449 (2020).